

Extraordinary alternating metal-insulator transitions in CaRuO_3 ultrathin films at integer multiples of 25 \AA of thickness

M. Sakoda^{1,*}, H. Nobukane^{2,3}, S. Shimoda⁴ and S. Tanda^{1,3}

¹*Department of Applied Physics, Graduate School of Engineering, Hokkaido University, Sapporo 060-8628, Hokkaido, Japan*

²*Department of Physics, Graduate School of Science, Hokkaido University, Sapporo 060-0810, Hokkaido, Japan*

³*Center of Education and Research for Topological Science and Technology, Hokkaido University, Sapporo, 060-8628, Hokkaido, Japan*

⁴*Institute for Catalysis, Hokkaido University, Sapporo 001-0021, Hokkaido, Japan*



(Received 10 March 2021; revised 25 October 2021; accepted 1 November 2021; published 17 November 2021)

Novel quantum phenomena, including high-temperature superconductivity, topological properties, and charge/spin density waves, appear in low-dimensional conductive materials. It is possible to artificially create low-dimensional systems by fabricating ultrathin films, quantum wires, or quantum dots with flat interfaces. We show that extraordinary metal-insulator transitions that oscillate depending on the scale occur in CaRuO_3 films with a thickness of around several unit cells. We grow high-crystalline CaRuO_3 ultrathin films, whose surface roughness is controlled at 199 pm, by molecular beam epitaxy. We observe that resistivity oscillates with a “magic” thickness of 25 \AA , and changes by three and nine orders of magnitude at room temperature and at low temperature, respectively. These changes are much larger than quantum size effects. We also confirm the same periodicity with photoelectron spectroscopy by etching the ultrathin film. Considering the large energy, periodicity, and anisotropy, we suggest that the oscillating transitions originate from the commensurability of Mott insulation triggered by Peierls instability.

DOI: [10.1103/PhysRevB.104.195420](https://doi.org/10.1103/PhysRevB.104.195420)

I. INTRODUCTION

In ultrathin films with a thickness of several nanometers, the degree of freedom of electrons is artificially enclosed in two dimensions. For example, quantum size effects appear in single element ultrathin films whose thicknesses are approximately of the order of de Broglie wavelengths [1–6]. Some experiments have been performed on ultrathin compounds of strongly correlated electron systems [7,8]. However, since it is technically difficult to control multiple elements precisely, most of the properties of artificially fabricated low-dimensional compounds fall into uncharted territory. It is necessary to develop ultrathin films with clear interfaces into compounds that have unique electronic states. Ruthenium oxides based on the RuO_6 octahedra layered structure contain a treasure chest of attractive physical properties including an anisotropic superconductor Sr_2RuO_4 [9], and Ca_2RuO_4 , which exhibits pressure-induced superconductivity and high- T_c superconductivity in thin flakes [10,11]. In addition, the layered compound $\text{Ca}_3\text{Ru}_2\text{O}_7$ is suggested to be a density wave state, and other combinations of RuO_6 conduction layers exhibit a variety of properties derived from the pseudo-two-dimensional nature [12–15]. In this study, we focus on CaRuO_3 , which has the simplest structure in Ca-Ru-O systems, as the target material for artificially fabricated low-dimensional electronic systems in ultrathin films.

CaRuO_3 has a GaFeO_3 -type crystalline structure consisting of a simple orthorhombic lattice (space group $Pbnm$) [16,17]

[Fig. 1(a)]. Since it does not have a layered compound, it shows isotropic conduction in three dimensions. CaRuO_3 is known to behave as a non-Fermi liquid at low temperatures, as seen in its electrical resistivity, magnetic susceptibility, and specific heat [18–25]. A narrow bandwidth of $\sim 20 \text{ meV}$ and a large effective mass of $\sim 4 m_0$ have also been observed [24,26]. From the above, CaRuO_3 is considered to be in the quantum critical region with strong electron correlation [22], and its physical properties are expected to change significantly depending on various external fields and states. CaRuO_3 has a pole Fermi surface (FS) and is expected to exhibit quantum phenomena based on two-dimensional (2D) electronic states in microphysical properties. In this study, the degrees of freedom of electrons are limited in real space by fabrication of ultrathin films of the strongly correlated compound and low-dimensional electron systems artificially appears. Our purpose is to explore the low-dimensional electronic properties that arise from a dual restriction imposed on the dimensions in wavenumber space by using a pole-shaped FS and in real space by using ultrathin films with clear interfaces. Since the Fermi wavelength of CaRuO_3 is as much as several nanometers [26], it is expected that scale-dependent quantum phenomena will appear in the ultrathin films.

Pure CaRuO_3 single crystals with a high residual resistivity ratio have been reported for bulk and thin films [27,28]. It has been shown that CaRuO_3 epitaxial thin films with few lattice defects can be produced by supplying sufficient oxygen [28,29]. In this paper, we develop high-quality CaRuO_3 ultrathin films with a stable supply of molecules by using molecular beam epitaxy (MBE) [30,31] [Fig. 1(b)] to investigate the phenomena that occur in artificially fabricated 2D electron systems.

*Corresponding author: sakodam@eng.hokudai.ac.jp

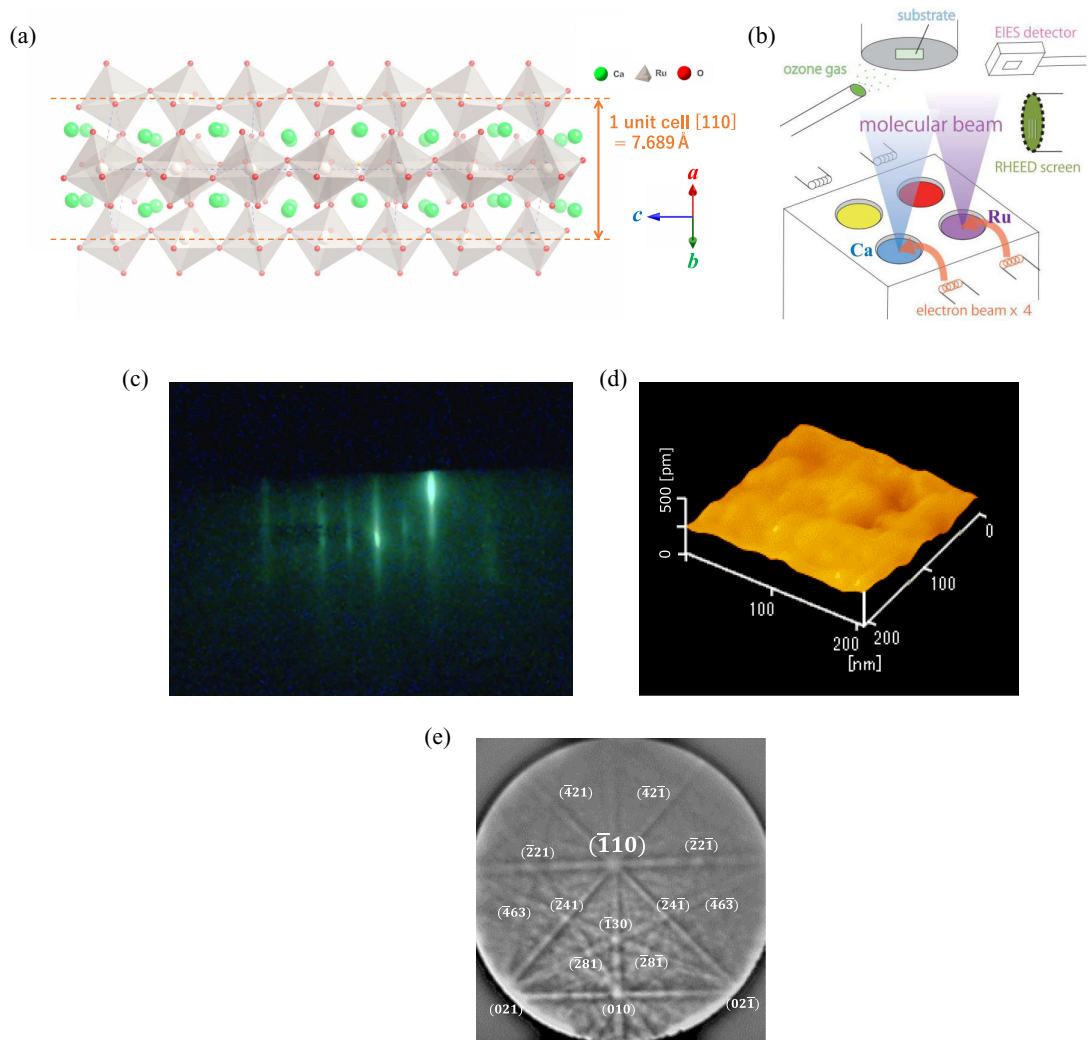


FIG. 1. (a) Crystal structure of CaRuO_3 grown on NdGaO_3 (110) substrate. (b) Schematic diagram of molecular beam epitaxy method. (c) RHEED pattern of 8 Å thick CaRuO_3 films. (d) Roughness of surface on 50 Å thick CaRuO_3 ultrathin film observed with AFM. (e) EBSD pattern of 50 Å thick CaRuO_3 film.

II. EXPERIMENTAL METHODS

A. Samples

Ultrathin films are prepared in a customer-designed MBE chamber (basal pressure of $\sim 5 \times 10^{-6}$ Pa). Molecular beams of Ru and Ca are controlled by electron impact emission spectroscopy (EIES). The molecular beam of CaF_2 is detected with a quartz crystal microbalance method in a constant power mode. The target rates of the molecular beam are Ru 0.1 Å/s, Ca 0.3 Å/s, and $\text{CaF}_2 \sim 1$ Å/s, respectively. The films are totally grown at rate of 25 Å/min. We determine the film thickness from the deposition time. The oxygen is supplied by O_3 using a conventional ozonizer. (The ozone concentration is about 14%.) The pressure of the O_2 in the chamber is monitored with a quadrupole mass electrometer (Q-mass). The growth condition is $\sim 2 \times 10^{-4}$ Torr for all the films. The growth temperature is 800 °C. The home-made MBE system is detailed elsewhere [30]. The substrate is NdGaO_3 (110) with a typical size of $\sim 3 \text{ mm} \times 6 \text{ mm}$. The surface roughness of the NdGaO_3 substrate is typically below 2.5 Å.

The CaRuO_3 films grow along the same crystal orientation as orthorhombic NdGaO_3 substrates because the lattice constant is very close to that of NdGaO_3 [31,32]. The high-quality epitaxial films are grown by the MBE method because the excess ruthenium supplied reevaporates as RuO_x in an oxygen atmosphere [30]. Since calcium has a high vapor pressure, the excess calcium supplied also re-evaporates from the substrate surface. Accordingly, both Ca and Ru are autoregulating constituent elements on epitaxial growth. We reproducibly fabricate pure and highly crystalline CaRuO_3 ultrathin films using a home-made MBE system [33] [Fig. 1(b)]. CaRuO_3 (110) is grown on a NdGaO_3 (110) substrate with crystal periodicity of 7.689 Å and containing two layers of RuO_6 octahedra [16,17] [Fig. 1(a)].

We deposit 50 Å of CaF_2 insulator as a barrier layer on CaRuO_3 ultrathin films below 20 °C as shown in the Supplemental Material [34]. It is difficult to measure the electrical resistivity of atomic layer films reproducibly without the barrier due to the high resistivity, which destroys the film surface in the atmosphere. The barriered films have less surface

roughness because they are not exposed to the atmosphere. We observe the surface of the films *in situ* using RHEED. The growth direction of CaRuO₃ (110) on the NdGaO₃ (110) substrate is confirmed by electron back-scattering diffraction (EBSD) as shown in Fig. 1(e).

B. Measurements

We employ the CaRuO₃ ultrathin film to measure the x-ray diffraction (XRD) shown in the Supplemental Material [34]. We also observe the surfaces of the films using field emission-scanning electron microscopy (FE-SEM; JSM-7000F, JEOL) and an atomic force microscope (AFM) (SPA-400). We measure the electrical properties in helium by using the conventional four-probe and two-probe methods for metal and insulating samples, respectively. The electrode is soldered with indium to destroy the CaF₂ barrier layer as shown in the Supplemental Material [34]. Some samples are measured at temperatures of as low as 0.5 K using a home-made ³He refrigerator. We also measure the electrical resistivity and Hall effect at temperatures as low as 2.2 K with a magnetic field of up to 6 T by using a physical property measurement system (PPMS, Quantum Design). The measurement setup is shown in the Supplemental Material [34] where a six-probe method is used to measure electrical resistivity and Hall effects. The UPS measurements and argon ion milling are performed with a JPS-9010MC (JEOL). The data are collected at room temperature with He I α ($h\nu = 21.2$ eV) photons. The energy resolution is set at 50 meV.

III. EXPERIMENTAL RESULTS

A. Sample configuration

When fabricating ultrathin films, it is important to control their thickness with a smaller than nanometer order. Figure 1(c) shows the reflection high-energy electron diffraction (RHEED) patterns of a CaRuO₃ film with a thickness of 8 Å. The sharp streak pattern is observed even in nanometer-thick films, which proves that the epitaxial films grow with a highly crystalline form and are flat with few impurities [28] (see the Supplemental Material [34]). The lattice matching between a NdGaO₃ substrate and CaRuO₃ is as small as 0.8% and 0.5% to the *c*-axis and another direction in the (110) plane, respectively. Furthermore, the oxygens in the RuO₆ octahedron are in matching positions. Consequently, the epitaxiality is excellent [31,32]. Growth reproducibility is also good, suggesting that the self-regulation of the elements of MBE is performed efficiently, and oversupplied Ca and Ru are reevaporated. Figure 1(d) shows the film surface observed with atomic force microscopy (AFM). The average surface roughness of CaRuO₃ ultrathin film is 199 pm, which is half the size of a RuO₆ conductive layer. Film thickness is confirmed using AFM, which is very accurate as it is within a few percent error compared to MBE molecular beam rate estimates (see the Supplemental Material [34]).

B. Electrical resistivity

We measure the electrical resistivity on CaRuO₃ ultrathin films at each thickness. Film with a conventional thickness of

504 Å has the same resistivity as the reported metal and is accompanied by a magnetic transition and non-Fermi liquid behavior [18–25] (see the Supplemental Material [34]). Surprisingly, the electrical resistivity of CaRuO₃ ultrathin films changes systematically by orders of magnitude. Figure 2(a) shows the temperature dependence of the electrical resistivity on CaRuO₃ ultrathin films with thicknesses between 101 and 85 Å. Film with a thickness of 101 Å is metallic, and the electrical resistivity increases exponentially as the film thickness decreases. Film with a thickness of 85 Å exhibits typical insulating behavior with maximum resistivities of 1×10^3 and 2×10^8 mΩcm at 300 and 4.2 K, respectively. The magnitudes of the electrical resistivity decrease again and revert to metallic behavior in the thinner films [Fig. 2(b)]. The magnitudes of the electrical resistivity on 71 Å thick CaRuO₃ ultrathin film are 3×10^{-1} and 7×10^{-2} mΩcm at 300 and 4.2 K, respectively. Despite there only being a slight difference between the sizes of the films with thicknesses of 71 and 85 Å, there is the large change in electrical resistivity of three orders of magnitude at room temperature and nine orders of magnitude or more at low temperature. The dependence of electrical resistivity on scale has not been reported for thick films or bulk samples on CaRuO₃. Figure 2(c) shows electrical resistivity as a function of temperature on CaRuO₃ ultrathin films grown with different thicknesses between 50 and 35 Å. The 50 Å thick film is metallic, and the electrical resistivity increases as the film thickness decreases. The 35 Å thick film exhibits its maximum electrical resistivity with an upturn in electrical resistivity below 70 K. The electrical resistivity in films less than 26 Å thick decreases again with typical metallic behavior [Fig. 2(d)]. The magnitudes of electrical resistivity increase or decrease systematically as the thin films become thinner. Since the magnitude of the Hall coefficient also corresponds to the electrical resistivity, the electronic state changes with film thickness (see the Supplemental Material [34]).

Figure 2(e) shows plots of electrical resistivity at 4.2 and 300 K on CaRuO₃ with different film thicknesses between 8 to 160 Å and a reference thickness of 504 Å. Figure 2(f) shows the corresponding plots of the sheet conductance to highlight the conductivity. It is noteworthy that semiconducting and metallic films appear alternately. The maximum resistivity/conductivity values are numbered in ascending order of film thickness and plotted against the film thickness [Fig. 2(g)]. The linearity fitting makes it clear that the electrical resistivity oscillates periodically depending on film thickness. The period estimated from the slopes of resistivity and conductivity are 25.1 ± 0.1 and 24.0 ± 1.2 Å, respectively. The “magic” thickness of 25 Å corresponds to three unit cells of CaRuO₃ (110) as shown in Fig. 1(a). The resistivity increases below the intercept thickness of ~ 10 Å in the fitting. The epitaxiality is confirmed from RHEED observations in the atomic layers [Figs. 1(c)] (see the Supplemental Material [34]). The lattice parameter of CaRuO₃ is 0.5% smaller in the [110] direction and 0.8% smaller in the [001] direction than that of NdGaO₃ substrate [35]. The crystal lattice in CaRuO₃ expands due to the significant influence of the epitaxial strain from the NdGaO₃ (110) substrate lattice over several atomic layers from the interface.

The temperature dependence of the electrical resistivity on the 85 Å thick film is well fitted by the variable range

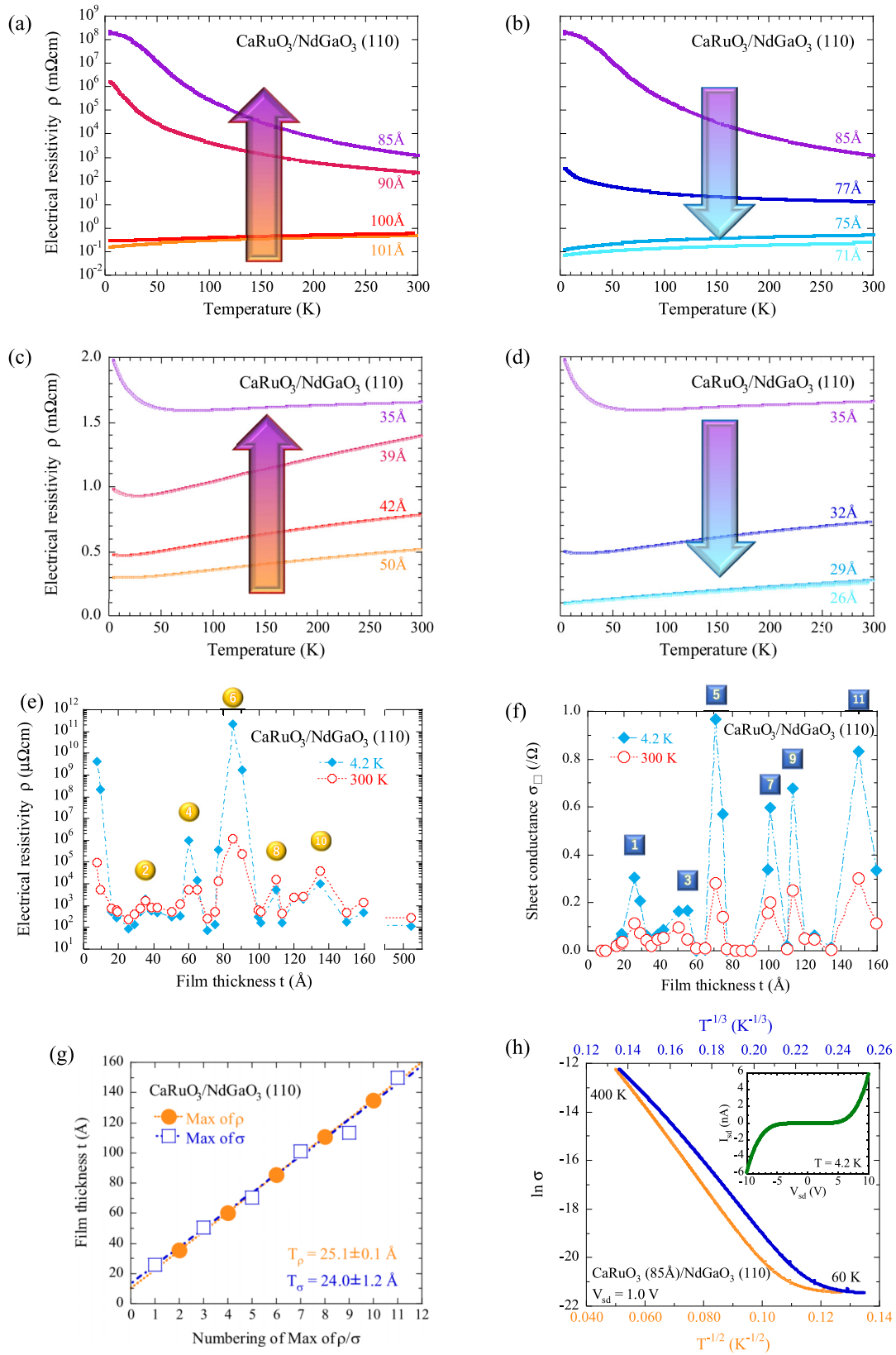


FIG. 2. Thickness dependence of electrical resistivity on CaRuO₃ ultrathin films. (a), (b) Electrical resistivity on CaRuO₃ thin films with thicknesses between 101 and 71 Å as a function of temperature. (c), (d) Electrical resistivity on CaRuO₃ thin films with thicknesses between 50 and 26 Å as a function of temperature. (e), (f) Electrical resistivity and sheet conductance as a function of thickness on CaRuO₃ films at 4.2 and 300 K, respectively. (g) Dependence of film thickness on maximum resistivity/conductance at low temperature. (h) Logarithm of electrical conductance as a function of $T^{-1/2}$ (lower), and $T^{-1/3}$ (upper) on 85 Å thick CaRuO₃ ultrathin film. The inset shows the current-voltage curve at 4.2 K.

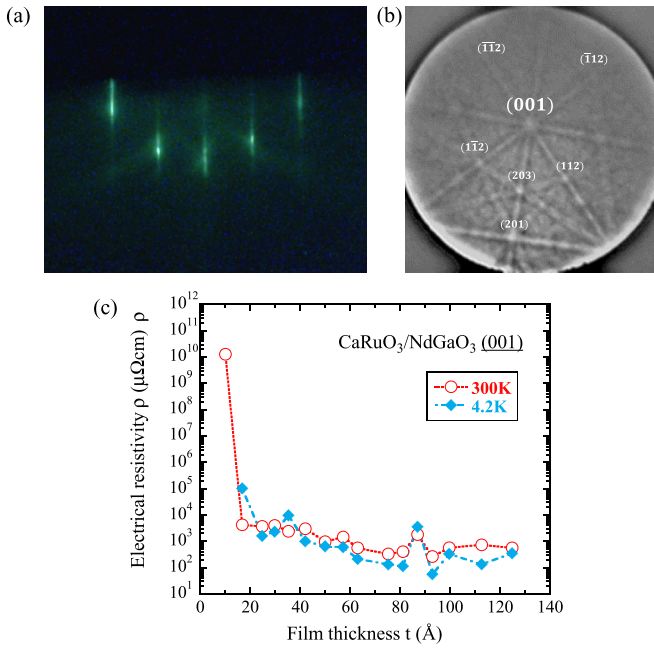


FIG. 3. Properties of CaRuO_3 (001) grown on NdGaO_3 (001) substrate. (a) RHEED pattern of CaRuO_3 (001) with thickness of 25 \AA . It shows a sharp streak pattern, which means a flat surface and high crystallinity. (b) EBSD pattern of 500 \AA thick CaRuO_3 (001) film. CaRuO_3 grows in the [001] crystal direction on a NdGaO_3 (001) substrate. (c) Electrical resistivity as a function of thickness at 300 K and 4.2 K.

hopping (VRH) of $\rho \sim \exp[(T_0/T)^{1/(d+1)}]$ with a large excitation energy of $T_0 \sim 26\,000$ K [Fig. 2(h)]. The exponential factor $d = 1$ proves that there is insulation with a strong Coulomb force. The large cyclotron effective mass observed thanks to the Shubnikov-de Haas effect [24] also indicates that CaRuO_3 has a heavy fermion state. CaRuO_3 is close to the quantum critical point to consider non-Fermi liquid behavior [19–26], which is adjacent to the Mott insulating phase. It can be interpreted to mean that CaRuO_3 is similar to the Mott insulator Ca_2RuO_4 [36].

C. Anisotropy of thickness dependence

We fabricated CaRuO_3 ultrathin films on NdGaO_3 (001) substrate to investigate the scale-dependent anisotropy. The epitaxiality of CaRuO_3 on NdGaO_3 (001) is excellent since a sharp streak pattern can be observed at a film thickness of 25 \AA similar to the growth on the NdGaO_3 (110) substrates [Fig. 3(a)]. The growth of (001) surface of CaRuO_3 is confirmed by EBSD [Fig. 3(b)]. We grow CaRuO_3 (001) ultrathin films with thickness of 10–125 \AA and measure the temperature dependence of electrical resistivity of each film. The electrical resistivity at 4.2 and 300 K is plotted for each film thickness [Fig. 3(c)]. The electrical resistivity of CaRuO_3 is extremely high at a film thickness of about 10 \AA , which is supposed to be due to the epitaxial strain from the substrate on the (001) growth causing the lattice to become larger as seen in the (110) growth. No alternations of the electrical resistance with a 25 \AA period are observed in the range of film thicknesses above 15 \AA . Namely, the metal-insulator transitions on

CaRuO_3 ultrathin films exhibit crystal anisotropy, and they are not seen or are greatly suppressed in the CaRuO_3 (001) ultrathin films on a NdGaO_3 (001) substrate. The crystal anisotropy of the quantum phase transition is thought to originate from the anisotropy of the electronic state. The anisotropic electronic state of low-dimensional FS is the key to the metal-insulator transitions.

D. Photoelectron spectroscopy

We perform ultraviolet photoelectron spectroscopy (UPS) on CaRuO_3 ultrathin film etched by using argon-ion milling *in situ* to reproduce the thickness dependence of the properties in one sample. Figure 4(a) shows the overall spectrum of the CaRuO_3 ultrathin film etched every second from 0 to 15 s. The initial film thickness is 110 \AA . The peak derived from the oxygen state seen around a binding energy (BE) of 5.6 eV is high in the nonetched film [37]. Considering the probe depth of a few angstroms realized with He I phonons, the calcium ions on the surface of the film form strong bonds with oxygen. It shows that the CaRuO_3 surface is oxidized by the atmosphere.

The valence band represents an insulating layer with low conduction. The oxygen peak becomes sharper after 1 s of etching. The noticeable increase in the valence band below 3 eV exhibits the CaRuO_3 spectrum. After 7 s of etching, the optical intensity reaches its maximum value. It starts to decrease after 8 s, and no change is observed after 11 s, which indicates that the CaRuO_3 is completely removed.

Figure 4(b) shows a close-up spectrum of another CaRuO_3 film with a BE between 0.5 and 3.5 eV to measure in detail the result for etching performed every half second. Etching tends to increase the intensity with good reproducibility compared with the previous sample. The optical intensity tends to increase with the etching time in the energy range of BE = 0.5–3.0 eV (see the Supplemental Material [34]). In general, as the thickness of the film becomes thinner, the conduction becomes lower, and thus the optical intensity decreases. The increase in its UPS intensity essentially indicates that the CaRuO_3 insulator is broken down and metallized. A crossover can be observed between 0.9 and 1.6 eV after 1.0–2.0 s of etching. The hump was reported to originate from Ru-4d electrons as observed by angle resolved photoelectron spectroscopy [26,38]. It has been reported that phonons, polarons, or magnons cannot contribute to the hump because of the large energy [38], which can be confirmed from the large T_0 .

Next, in Fig. 2 we confirm the reproduction of the film thickness dependence of the electrical conduction in terms of optical conductivity. Figure 4(c) compares the sheet conductance as a function of thickness at 300 K and the optical intensity of UPS at 1.1 eV as a function of etching time. The arrows represent the coincidence between the increase in optical intensity and the peak of the electrical conduction at etching time $t = 1.0, 4.0,$ and 6.0 s. Finally, it is reproducibly proven on one etched film that the periodicity of the thickness in terms of optical intensity is the same as that for electrical conductivity. The periodicities show good agreement at BE = 1.1 eV where the hump is prominent, which reveals that suppression on the Ru-4d orbital is related to insulation.

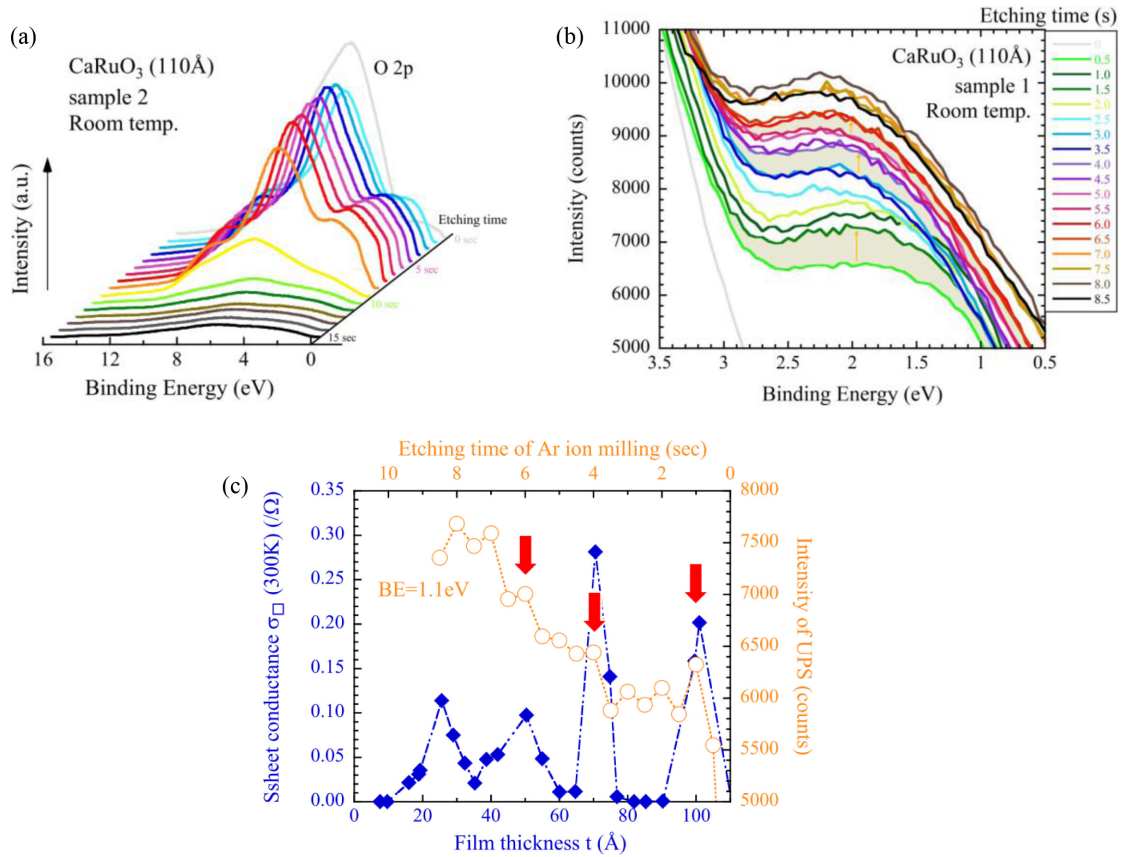


FIG. 4. Correspondence of periodic transitions in optical intensity to a CaRuO₃ ultrathin film etched by argon ion milling. (a) Overall UPS spectra of 110 Å thick CaRuO₃ ultrathin film etched from 0 to 15 s *in situ*. (b) Details of spectra with BE between 0.5 and 3.5 eV of another 110 Å thick CaRuO₃ ultrathin film etched every 0.5 s from 0 to 8.5 s. The shaded area highlights the large increase in optical conductivity. (c) Comparison of electrical conductance as a function of film thickness and optical intensity as a function of etching time. The arrows indicate the correspondence to the periodicity of the oscillating transitions.

IV. DISCUSSION

What is the mechanism of the metal-insulator transitions that oscillate with thickness? The important features are that (1) the transitions alternate with the magic thickness period of 25 Å corresponding to three times the thickness of a CaRuO₃ (110) unit cell, (2) the transitions are accompanied by a large excitation energy equivalent to a few electron volts, and (3) anisotropy, namely, they can be clearly seen only in CaRuO₃ (110) growth. Until now, it has been believed that oscillations of properties depending on scale are caused by quantum size effects [1–3]. CaRuO₃ ultrathin films form typical one-dimensional quantum wells sandwiched by the substrates and barriers. However, the activation energy that accompanies metal-insulator transitions is too large to be interpreted as quantum wells within a bandwidth as small as ~ 200 meV in CaRuO₃ [26]. Therefore, the size effect caused by the quantum wells does not dominate the scaling dependence in this paper. When the strong Coulomb interaction in the quantum critical phase is taken into consideration, it is necessary to discuss the Mott insulation for a large excitation energy. The Fermi wavelength of the cylindrical FS in the [110] direction has been observed between 22 and 33 Å in ARPES experiments [26].

Although typical Mott insulators appear in half filling bands, compounds that have no half filling bands also become

Mott insulators as a result of the stripe correlations of spins and carriers [39]. The concept of commensurability on stripe Mott insulation is suitable for 2D systems with several unit cells. It is considered that the Mott insulation on CaRuO₃ (110) ultrathin films is dependent on the commensurability on stripe correlations when the thickness is a multiple of three unit cells [Figs. 5(a) and 5(c)]. Considering the period of 25 Å for the oscillating transitions, it is assumed that there is a single RuO₆ layer of domain wall for every three unit cells. The other RuO₆ layers form the Mott insulator with antiferromagnetism. Since electrons are left over except for the multiple of the magic thickness, the Mott insulating stripe on CaRuO₃ is dissolved and reverts to metal [Fig. 5(b)].

The stripe correlations of spins and carriers with three time periods are triggered by Peierls instability [40–44]. CaRuO₃ consists of a square pole FS [26], which is advantageous for nesting properties. Since the wavenumber $k_{[110]}$ of the FS corresponds to one-third of the Brillouin zone, the energy gain from the stabilization of Peierls transition is large enough to form a period of 25 Å in real space. The Peierls instability is proven by the anisotropy of the metal-insulator transitions. They are clearly observed on CaRuO₃ (110) where the nesting property is excellent in the growth direction. By contrast, they can be hardly seen on CaRuO₃ (001) films where the pole FS has an open orbit in the growth direction [001], i.e., it cannot

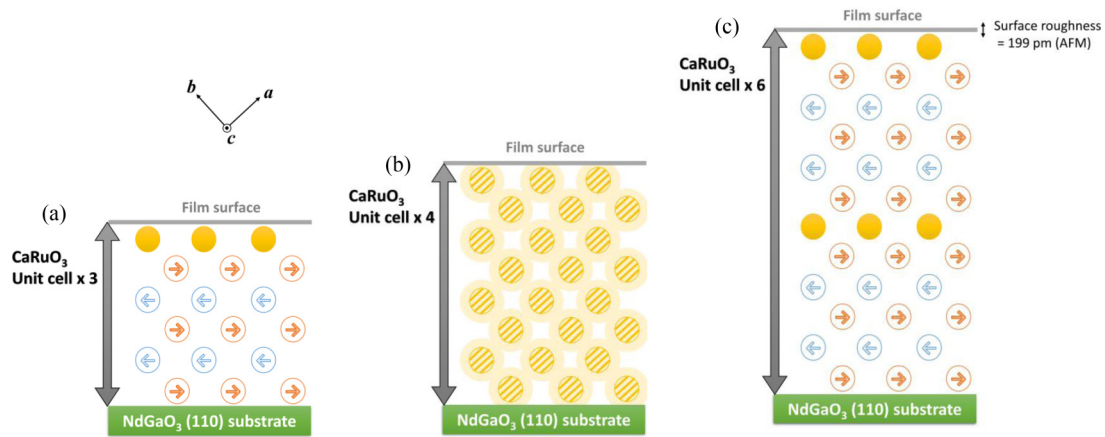


FIG. 5. Commensurability schematic of Mott insulation on CaRuO_3 (110) ultrathin films. The film thicknesses are (a) three units, (b) four units, and (c) six units. The circles indicate the Ru ions. The closed circles indicate the domain walls occupied by electrons or holes. The open circles indicate the Mott insulating localized electrons. The arrows indicate the antiferromagnetism state. The circles with diagonal lines indicate the metallic state of nonfilled bands.

take any nesting vectors. This is definitive proof that the size effect is related to this anisotropic Fermi surface.

Namely, the metal-insulator transitions are caused by the dimensional restrictions in different directions caused by each 2D-FS and the ultrathin films. The metal-insulator transitions can be rephrased as the incommensurability-commensurability transitions that occur only under clear boundary conditions. No scaling dependences on CaRuO_3 have been discovered in thick films or bulk samples because of the mean free path of electrons.

Finally, we will also mention other possible mechanisms. There is a possibility that the Kondo effect caused by Ru impurities may appear [45], and that Anderson localization is enhanced in the 2D state by ultrathin films [46]. However, we considered the large changes in electrical resistivity and eliminated the possibility that these were the nature of the scale dependence. The RHEED patterns at each film thickness removed the possibility of structural transition. Pressure experiments [10] and thin films [11] on Ca_2RuO_4 have shown that the metal-insulator transition is closely related to the lattice. Assuming that the Mott-Hubbard model can be applied to the novel size effect of CaRuO_3 , it is consistent the metal-insulator transition will involve a change in the lattice.

V. SUMMARY

We grew CaRuO_3 ultrathin films with the MBE method. We have fabricated thin films that exhibit sharp streak patterns of RHEED at thicknesses above 8 Å. The AFM observation

shows that their surface roughness was controlled at 199 pm. We measured the temperature dependence of the electrical resistivity at each film thickness and found that the magnitude of the electrical resistivity changes systematically. We observed that electrical resistivity oscillates with a thickness of 25 Å, and changes by three and nine orders of magnitude at room temperature and at low temperature, respectively. We observed the same periodicity with UPS by etching the ultrathin film. We establish “scales” as a new parameter for quantum phase transitions following the angle [47].

ACKNOWLEDGMENTS

The authors thank Prof. M. Naito, K. Ichimura, R. Suzuki, N. Matsunaga, T. Kurosawa, Dr. Y. B. Nanao, and K. Nakatsugawa for valuable discussions and support. Part of this work was conducted at the Laboratory of XPS Analysis, Joint-use Facilities, Hokkaido University. The Open Facility of the Institute for Catalysis was used for the UPS. This study is financially supported by the Takahashi Industrial and Economic Research Foundation, Japan Prize Foundation, Murata Science Foundation, Yashima Environment Technology Foundation, Inamori Foundation, Iketani Science and Technology Foundation, Samco Science and Technology Foundation, Foundation for Interaction in Science & Technology, Izumi Science and Technology Foundation, Ito Science Promotion Association, and Sumitomo Electric Group SRC Foundation, and Nippon Sheet Glass Foundation for Material Science and Engineering.

- [1] V. B. Sandomirskii, *Sov. Phys. JETP* **25**(1), 101 (1967).
 [2] Y. F. Ogrin, V. N. Lutskii, M. U. Arifova, V. I. Kovalev, V. B. Sandomirskii, and M. I. Elinson, *Sov. Phys. JETP* **26**(4), 714 (1968).
 [3] H. T. Chu, P. N. Henriksen, and J. Alexander, *Phys. Rev. B* **37**, 3900 (1988).
 [4] M. Jalochowski and E. Bauer, *Phys. Rev. B* **38**, 5272 (1988).

- [5] Y.-S. Fu, S. H. Ji, X. Chen, X. C. Ma, R. Wu, C. C. Wang, W. H. Duan, X. H. Qiu, B. Sun, P. Zhang, J. F. Jia, and Q. K. Xue, *Phys. Rev. Lett.* **99**, 256601 (2007).
 [6] S. Sakuragi, T. Sakai, S. Urata, S. Aihara, A. Shinto, H. Kageshima, M. Sawada, H. Namatame, M. Taniguchi, and T. Sato, *Phys. Rev. B* **90**, 054411 (2014).

- [7] Y. J. Chang, C. H. Kim, S. H. Phark, Y. S. Kim, J. Yu, and T. W. Noh, *Phys. Rev. Lett.* **103**, 057201 (2009).
- [8] H. Shishido, T. Shibauchi, K. Yasu, T. Kato, H. Kontani, T. Terashima, and Y. Matsuda, *Science* **327**, 980 (2010).
- [9] Y. Maeno, H. Hashimoto, K. Yoshida, S. Nishizaki, T. Fujita, J. G. Bednorz, and F. Lichtenberg, *Nature (London)* **372**, 532 (1994).
- [10] P. L. Alireza, F. Nakamura, S. K. Goh, Y. Maeno, S. Nakatsuji, Y. T. C. Ko, M. Sutherland, S. Julian, and G. G. Lonzarich, *J. Phys.: Condens. Matter* **22**, 052202 (2010).
- [11] H. Nobukane, K. Yanagihara, Y. Kunisada, Y. Ogasawara, K. Isono, K. Nomura, K. Tanahashi, T. Nomura, T. Akiyama, and S. Tanda, *Sci. Rep.* **10**, 3462 (2020).
- [12] S. N. Ruddlesden and P. Popper, *Acta Crystallogr.* **11**, 54 (1958).
- [13] H. K. Muller-Buschbaum and J. Wilkens, *Z. Anorg. Allg. Chem.* **591**, 161 (1990).
- [14] M. Itoh, M. Shikano, and T. Shimura, *Phys. Rev. B* **51**, 16432 (1995).
- [15] F. Baumberger, N. J. C. Ingle, N. Kikugawa, M. A. Hossain, W. Meevasana, R. S. Perry, K. M. Shen, D. H. Lu, A. Damascelli, A. Rost, A. P. Mackenzie, Z. Hussain, and Z.-X. Shen, *Phys. Rev. Lett.* **96**, 107601 (2006).
- [16] A. Kanbayasi, *J. Phys. Soc. Jpn* **44**, 108 (1978).
- [17] W. Bensch, H. W. Schmalle, and A. Reller, *Solid State Ion.* **43**, 171 (1990).
- [18] S. C. Gausepohl, M. Lee, R. A. Rao, and C. B. Eom, *Phys. Rev. B* **54**, 8996 (1996).
- [19] L. Klein, L. Antognazza, T. H. Geballe, M. R. Beasley, and A. Kapitulnik, *Phys. Rev. B* **60**, 1448 (1999).
- [20] Y. S. Lee, J. Yu, J. S. Lee, T. W. Noh, T. H. Gimm, H. Y. Choi, and C. B. Eom, *Phys. Rev. B* **66**, 041104(R) (2002).
- [21] P. Khalifah, I. Ohkubo, H. M. Christen, and D. G. Mandrus, *Phys. Rev. B* **70**, 134426 (2004).
- [22] G. Cao, O. Korneta, S. Chikara, L. E. DeLong, and P. Schlottmann, *Solid State Commun.* **148**, 305 (2008).
- [23] S. Tripathi, R. Rana, S. Kumar, P. Pandey, R. S. Singh, and D. S. Rana, *Sci. Rep.* **4**, 3877 (2014).
- [24] M. Schneider, D. Geiger, S. Esser, U. S. Pracht, C. Stingl, Y. Tokiwa, V. Moshnyaga, I. Sheikin, J. Mravlje, M. Scheffler, and P. Gegenwart, *Phys. Rev. Lett.* **112**, 206403 (2014).
- [25] G. Koster, L. Klein, W. Siemons, G. Rijnders, J. S. Dodge, C. B. Eom, D. H. A. Blank, and M. R. Beasley, *Rev. Mod. Phys.* **84**, 253 (2012).
- [26] Y. Liu, H. P. Nair, J. P. Ruf, D. G. Schlom, and K. M. Shen, *Phys. Rev. B* **98**, 041110(R) (2018).
- [27] A. Koriyama, M. Ishizaki, T. C. Ozawa, T. Taniguchi, Y. Nagata, H. Samata, Y. Kobayashi, and Y. Noro, *J. Alloys Compd.* **372**, 58 (2004).
- [28] H. P. Nair, Y. Liu, J. P. Ruf, N. J. Schreiber, S. L. Shang, D. J. Baek, B. H. Goodge, L. F. Kourkoutis, Z. K. Liu, K. M. Shen, and D. G. Schlom, *APL Mater.* **6**, 046101 (2018).
- [29] G. N. Daptary, C. Sow, S. Sarkar, S. Chiniwar, P. A. Kumar, A. Sil, and A. Bid, *Physica B Condens. Matter* **511**, 74 (2017).
- [30] M. Naito, H. Sato, A. Tsukada, and H. Yamamoto, *Physica C Supercond.* **546**, 84 (2018).
- [31] S. Geller, *Acta Crystallogr.* **10**, 243 (1957).
- [32] M. Sasaura, S. Miyazawa, and M. Mukaida, *J. Appl. Phys.* **68**, 3643 (1990).
- [33] L. Esaki and R. Tsu, *IBM J. Res. Dev* **14**, 61 (1970).
- [34] See Supplemental Material at <http://link.aps.org/supplemental/10.1103/PhysRevB.104.195420> for sample preparation, additional RHEED pictures, resistivity, Hall effect, and UPS results.
- [35] R. Rao, Q. Gan, C. B. Eom, R. J. Cava, Y. Suzuki, J. J. Krajewski, S. C. Gausepohl, and M. Lee, *Appl. Phys. Lett.* **70**, 3035 (1997).
- [36] S. Nakatsuji, V. Dobrosavljevic, D. Tanaskovic, M. Minakata, H. Fukazawa, and Y. Maeno, *Phys. Rev. Lett.* **93**, 146401 (2004).
- [37] K. Maiti and R. S. Singh, *Phys. Rev. B* **71**, 161102(R) (2005).
- [38] H. F. Yang, C. C. Fan, Z. T. Liu, Q. Yao, M. Y. Li, J. S. Liu, M. H. Jiang, and D. W. Shen, *Phys. Rev. B* **94**, 115151 (2016).
- [39] J. M. Tranquada, B. J. Sternlieb, J. D. Axe, Y. Nakamura, and S. Uchida, *Nature (London)* **375**, 561 (1995).
- [40] S. Biermann, A. Poteryaev, A. I. Lichtenstein, and A. Georges, *Phys. Rev. Lett.* **94**, 026404 (2005).
- [41] M. W. Haverkort, Z. Hu, A. Tanaka, W. Reichelt, S. V. Streltsov, M. A. Korotin, V. I. Anisimov, H. H. Hsieh, H. J. Lin, C. T. Chen, D. I. Khomskii, and L. H. Tjeng, *Phys. Rev. Lett.* **95**, 196404 (2005).
- [42] T. C. Koethe, Z. Hu, M. W. Haverkort, C. Schüßler-Langeheine, F. Venturini, N. B. Brookes, O. Tjernberg, W. Reichelt, H. H. Hsieh, H.-J. Lin, C. T. Chen, and L. H. Tjeng, *Phys. Rev. Lett.* **97**, 116402 (2006).
- [43] M. M. Qazilbash, M. Brehm, B.-G. Chae, P.-C. Ho, G. O. Andreev, B.-J. Kim, S. J. Yun, A. V. Balatsky, M. B. Maple, F. Keilmann, H.-T. Kim, and D. N. Basov, *Science* **318**, 1750 (2007).
- [44] P. Monceau, *Adv. Phys.* **61**, 325 (2012).
- [45] J. Kondo, *Prog. Theor. Phys.* **32**, 37 (1964).
- [46] P. Anderson, *Phys. Rev.* **109**, 1492 (1958).
- [47] Y. Cao, V. Fatemi, S. Fang, K. Watanabe, T. Taniguchi, E. Kaxiras, and P. Jarillo-Herrero, *Nature (London)* **556**, 43 (2018).